PAPER

Check for updates

A hollow MnO₂ nanozymes empowered injectable hydrogel for intrauterine adhesion therapy by alleviating oxidative stress and promoting endometrial repair

Ying Xu,†[a] Zi Ye,†[a,b] Sentao Hu,[a,b] Lichao Chu,[a] Liaobing Xin,*[b] Wangyan He,[a] Weijun Tong, [ID] *[a] Songying Zhang*[b] and Lie Ma [ID] *[a,b]

Intrauterine adhesion (IUA) is an important cause of infertility and poses a challenge to women's reproductive health. However, conventional clinical treatments fail to fundamentally repair the function of the endometrium. While stem cell therapy is a promising breakthrough in IUA treatment, its clinical application remains limited. Recent studies have highlighted the pivotal roles of oxidative stress and inflammatory immune responses in IUA pathogenesis, underlining the requirement for excessive reactive oxygen species (ROS)-scavenging ability, where nanozymes demonstrated distinctive advantages. Herein, we report the preparation of a nanozyme-powered injectable hydrogel (HME) by integrating hollow estradiol-loaded MnO₂ nanoparticles (MnO₂@E2 NPs) with a hyaluronic acid-based hydrogel to explore its therapeutic effect in IUA. *In vitro* studies demonstrated that MnO₂@E2 NPs exhibited catalase (CAT)-like and superoxide dismutase (SOD)-like enzymatic activities, effectively scavenging ROS. The HME possessed optimal mechanical properties, biocompatibility, robust antioxidant activities and regulatory properties on macrophages, thereby protecting human endometrial stromal cells (HESCs) and enhancing their proliferation. In a rat endometrial injury model, HME treatment regulated the uterine inflammatory microenvironment, suppressed M1 macrophage expression and further promoted endometrial repair. In conclusion, the HME offers a novel and effective therapeutic approach for IUA, with potential clinical implications for women of reproductive age.

1. Introduction

Intrauterine adhesion (IUA), which is an important cause of female infertility, refers to the condition in which the basal layer of the endometrium is damaged and replaced by inactive fibrotic tissue.[1] The clinical treatment for IUA is hysteroscopic adhesiolysis combined with physical barriers such as intrauterine devices and uterine balloons, along with oral estrogen therapy.

The primary biological processes for the repair of the endometrium include influx of inflammatory cells, re-epithelialization and remodeling of the ECM.[2] Traditional clinical treatments only focus on physical isolation, thus failing to regenerate the endometrium radically. In contrast, cutting-edge research has regarded immune regulation and remodeling of endometrial tissues as critical factors, resulting in the development of stem cell therapy.[3,4] In our previous research,[5] a construct of an umbilical cord-derived mesenchymal stromal cell (UC-MSC)-laden collagen scaffold (CS/UC-MSCs) was applied for IUA treatment, where UC-MSCs can exert effects through paracrine action, resulting in favorable efficacy on IUA. In case of side effects resulting from stem cell differentiation, researchers applied acellular therapy such as introducing stem cell derivatives for the treatment of IUA. For example, based on CS/UC-MSCs, we replaced UC-MSCs with exosomes (Exos) secreted by UC-MSCs through paracrine action and obtained CS/Exos,[6] which exhibited a more effective and safe effect. However, the transformation cycle of the use of active factors is long and costly, and thus, new methods still need to be developed.

The main pathogenesis-based cause of IUA is mechanical injury of the endometrium.[7] After suffering damage, the endometrial microenvironment produces excessive reactive oxygen

[a]*MOE Key Laboratory of Macromolecular Synthesis and Functionalization, Department of Polymer Science and Engineering, Zhejiang University, Hangzhou 310058, China. E-mail: liema@zju.edu.cn, tongwj@zju.edu.cn*
[b]*Key Laboratory of Reproductive Dysfunction Management of Zhejiang Province, Assisted Reproduction Unit, Department of Obstetrics and Gynecology, Sir Run Run Shaw Hospital, School of Medicine, Zhejiang University, Hangzhou 310016, China. E-mail: zhangsongying@zju.edu.cn, xlbing01@163.com*
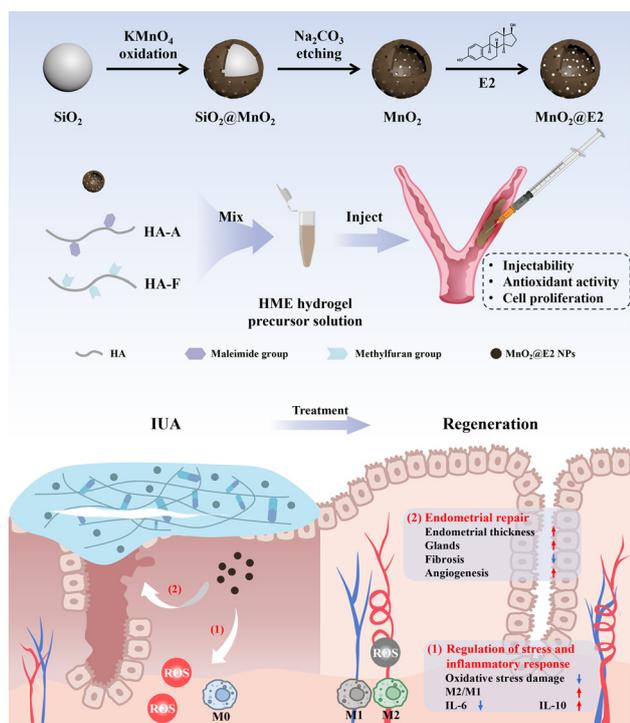† Co-first author.

species (ROS). Elevated levels of ROS may disrupt the endogenous antioxidant system, contributing to oxidative stress, triggering abnormal inflammatory responses,[8] and further inducing the aggregation of immune cells such as macrophages and releasing inflammatory cytokines, for instance, IL-1β and TNF-α.[9,10] If the transition from the inflammatory stage to the proliferative and remodeling stage does not occur in time, functional loss of the endometrium may occur.[1] Therefore, alleviating excessive ROS can effectively achieve the purpose of regulating immune inflammatory responses.

The application of ROS-scavenging biomaterials is an effective therapeutic approach to alleviate oxidative stress damage. Some studies have modified biomaterial systems and added active antioxidant molecules to endow them with antioxidant capacity.[11,12] Another more controllable strategy is to prepare nanozyme composite material systems.[13,14] Nanozymes are inorganic nanomaterials that can simulate multiple catalytic abilities, compensating for the poor stability and single antioxidant property of other methods, and thus having research potential. The common types of nanozymes mainly include metal-based (Mn-based[15] and Ce-based[16] nanostructures), carbon-based (carbon quantum dots[17]) and metal–organic framework (MOF)-based (ZIF-8[18]) nanozymes.[19] Nanozymes have been proven effective in the treatment of numerous inflammatory diseases, for instance, myocardial injury[20,21] and inflammatory bowel disease.[22,23] However, research involving nanozymes in the field of reproductive repair is relatively limited and thus deserves further exploration.

The residence time of nanozymes in the uterus is relatively short in comparison with the requirement. Hence, many studies have combined drug-loaded nanozymes with carriers to prolong the treatment time. Compared with clinical materials, injectable hydrogels have advantages such as appropriate mechanical modulus, shape adaptability, and injectability. In our previous study,[24] a covalently cross-linked hyaluronic acid (HA) hydrogel was prepared through the Diels–Alder (D–A) reaction, and UC-MSCs were loaded into the hydrogels, successfully achieving injectability and promoting endometrial regeneration. The D–A reaction is a type of click reaction, which requires simple reaction conditions and does not produce by-products, demonstrating unique bioorthogonality. HA is an important component of the extracellular matrix and mediates crucial physiological functions in the body, which is often used as an adhesion barrier after surgery.[25,26]

In this study, a collaborative delivery therapy platform was prepared for the adjustment of the uterine microenvironment and further remodeling of endometrial functionalization after IUA (Scheme 1). Firstly, we designed hollow MnO₂ nanoparticles (NPs) with enzyme-like activities and loaded the drug β-estradiol (E2) to prepare MnO₂@E2 NPs. E2 is a type of natural estrogen, which possesses strong biological activity for promoting endometrial proliferation angiogenesis, which has been widely applied in the treatment of IUA.[27–29] Then, MnO₂@E2 NPs were mixed with maleimide-modified hyaluronic acid (HA-A) and methylfuran-modified hyaluronic acid (HA-F), and injected into the uterus via a minimally invasive method to form a hydrogel in situ. In vitro and in vivo experiments revealed that in the active phase of inflammation, while the system served as a physical isolation barrier, MnO₂ eliminated excessive ROS and inhibited abnormal inflammatory responses by decreasing M1 macrophage polarization. Besides, the sustained-release E2 from the hydrogel promoted the later recovery of physiological functions. The hydrogel realized in situ drug administration and covered the entire immune stage, achieving precise treatment in both spatial and temporal dimensions. This nanozyme-powered hydrogel provides a novel strategy for the structural and functional repair of the endometrium after IUA, and has the value of further research.

2. Experimental section

2.1. Synthesis of MnO₂ and MnO₂@E2 NPs

SiO₂ NPs were synthesized by hydrolyzing TEOS using the Stober method,[30] and the synthesis processes for MnO₂ and MnO₂@E2 NPs are described in the SI.

2.2. Preparation and characterization of the HME

HA-A and HA-F were prepared in accordance with the reported method,[24] which is displayed in the SI.

The degree of substitution of maleimide or methylfuran groups was determined by proton nuclear magnetic resonance spectroscopy (¹H NMR, AVANCE III 500, Bruker, Germany). 3.5 wt% HA-A and HA-F solutions (1:1, v/v) and

Scheme 1 Schematic of the hollow MnO₂ nanozymes empowered injectable hydrogel (HME) for endometrial repair in IUA.

MnO$_2$@E2 mother liquor were mixed at 37 °C to form a hydrogel. The hydrogel without nanoparticles was named H, the hydrogel with MnO$_2$ NPs was named HM, and the hydrogel doped with 200 μg mL^{-1} MnO$_2$@E2 NPs was named HME200. The fracture morphology of the hydrogel was characterized by SEM. The basic physicochemical properties of the hydrogels were tested as follows.

Rheological properties. The rheological behavior of the hydrogels was investigated using a rotational rheometer (Mars 60, Haake, Germany). Time scanning was performed to characterize the crosslinking process with a 35 mm parallel plate, applying a strain amplitude of 1% and a frequency of 1 Hz at 37 °C. Frequency scanning was exerted with a diameter of 20 mm and height of 2 mm under a 20 mm parallel plate with a strain amplitude of 1% and a frequency range of 0.01–100 rad s^{-1} at 25 °C.

Mechanical properties. The stress–strain curves of the hydrogels were measured using a mechanical testing machine (AGS-X-10kN, Shimadzu, Japan), and the strain curves ranging from 5–10% were selected to calculate the compression moduli.

Drug release property. The hydrogel was added to a dialysis bag (M_w = 8–14 kDa), which was immersed in 10 mL PBS (pH = 7.4, 0.1% Tween 80), and incubated at 37 °C for 120 rpm (r). The following steps were the same as those for the drug release test of MnO$_2$@E2 NPs.

2.3. Antioxidant properties

H$_2$O$_2$ removal. The hydrogels were immersed in 100 μM H$_2$O$_2$ (200 μL hydrogel per mL) and incubated at 37 °C and 120 r for 4 h. The following steps were the same as those for MnO$_2$@E2 NPs.

Inhibition of ·O$_2^-$. The hydrogels were immersed in a mixture of L-methionine (65 mM), riboflavin (100 μM) and NBT (375 μM) (200 μL hydrogel per mL) and irradiated with a white light lamp for 30 min. The absorbance of the supernatant was measured at 560 nm using an ultraviolet-visible spectrophotometer (UV-Vis, UH5300, Hitachi, Japan).

Scavenging of 1,1-diphenyl-2-trinitrophenylhydrazine radical (DPPH·). The hydrogels were immersed in 100 μM DPPH ethanol solution (400 μL hydrogel per mL) and incubated at 37 °C, 120 r for 4 h. The absorbance of the supernatant was measured at 517 nm.

Scavenging of 2,2′-azino-bis(3-ethylbenzothiazoline-6-sulfonic acid) radical cation (ABTS·$^+$). The experiment was conducted using the Total Antioxidant Capacity Assay Kit with ABTS method (Beyotime, Shanghai, China). The hydrogels were immersed in the ABTS working solution (250 μL hydrogel per mL) and incubated at 37 °C, 120 r for 30 min. The absorbance was measured at 734 nm.

2.4. Cell isolation and culture

All the procedures were approved by the Ethics Committee of Sir Run Run Shaw Hospital, Zhejiang University School of Medicine (Ethics Number: SRRSH202402295). Written informed consents were obtained from all patients prior to tissue collection of human endometrial stromal cells (HESCs). Endometrial samples were collected from healthy women aged 25–40 years who underwent hysteroscopic endometrial biopsy 3–7 days after the completion of menstruation. HESCs were isolated from the endometrial specimens according to the previously reported method.[31]

2.5. *In vitro* cytocompatibility

The cytocompatibility of the hydrogels was evaluated based on the cell viability of HESCs cultured with an extract of the hydrogel. The extract was prepared by soaking the hydrogel in DMEM/F12 medium (0.1 g hydrogel per mL) at 37 °C for 24 h. HESCs were cultured with the extract at a seeding density of 8 × 10^3 cells per well for 1, 2 and 3 d. At the preset times, the cell viability was tested using Cell Counting Kit-8 (CCK-8, TargetMol, USA) and the absorbance at 450 nm was measured using a microplate reader (Multiskan FC, USA).

Bone marrow-derived macrophages (BMDMs) were extracted from the bone marrow of female C57BL/6 mice (6 weeks old) and cultured in 1640 medium containing 20 ng mL^{-1} granulocyte-macrophage colony-stimulating factor (GM-CSF, Novoprotein, CK02) for 5 days.

2.6. Intracellular antioxidation properties

Selection of H$_2$O$_2$ concentration. HESCs were cultured with medium containing 50 μM, 100 μM, and 200 μM H$_2$O$_2$ for 24 h. The cell viability was tested using the CCK-8 method.

The protective effect of HME on HESCs under H$_2$O$_2$ conditions. After seeding and attachment, HESCs were cultured with the hydrogels using a Transwell system with DMEM/F12 medium supplemented with H$_2$O$_2$. The experimental groups were set as follows: ① Control group: no H$_2$O$_2$ was added; ② H$_2$O$_2$ group: no treatment was applied; ③ H group: 100 μL of H precursor solution; ④ HM group: 100 μL of HM precursor solution; and ⑤ HME group: 100 μL of HME precursor solution (the content of MnO$_2$ in the HM and HME groups was the same, and this was also the case in the following experiments). After 3 days, the cell viability was tested using the CCK-8 method.

Intracellular scavenging of ROS. After seeding and attachment in a 6-well plate, HESCs were cultured with the hydrogels using a Transwell system with 2 mL per well medium supplemented with 100 μM H$_2$O$_2$. The experimental groups were the same as above, and the volume of the hydrogel precursor solution was 200 μL. After culturing at 37 °C for 24 h, medium containing 2.5 μM CM-H$_2$DCFDA probe (Beyotime, Shanghai, China) was added and incubated at 37 °C in the dark for 30 min. Subsequently, HESCs were trypsinized and centrifuged for detection by a flow cytometer (CytoFLEX, Beckman Coulter, USA).

Intracellular reduction of oxidative stress damage. HESCs were seeded in a 12-well plate pre-laid with cell climbing sheets. HESCs were cultured with the hydrogel in a Transwell chamber under the conditions of 100 μM H$_2$O$_2$ for 24 h. Groups were set as the experiment of intracellular ROS scavenging. After fixation and blocking, cells were incubated with

4-hydroxynonenal primary antibody (4-HNE, 1 : 50, Invitrogen, MA5-27570), Alexa Fluor 488 labeled goat anti-mouse secondary antibody (1 : 500, Invitrogen, A-11029) and Hoechst (1 : 500, Invitrogen, H3570) in turn. Fluorescence images were captured under a confocal fluorescence microscope (CFM, LSM800, Carl Zeiss, Germany).

2.7. Intracellular regulatory effect on the phenotype of macrophages

BMDMs were treated with the hydrogels using a Transwell system for 6 h, followed by the addition of 200 ng mL^{-1} LPS to induce an inflammatory model (M1) for 18 h. The experimental groups were set as follows: ① Control group: no LPS was added; ② LPS group: no treatment was applied; ③ H group; ④ HM group; and ⑤ HME group. The following experimental methods were adopted to characterize their properties.

Flow cytometry. Cells were stained with antibodies including anti-Mo F4/80 FITC (eBioscience, 11-4801-82), anti-Mo CD86 (eBioscience, 12-0862-82) and anti-Mo CD206 PE-Cy7 (BioLegend, 141720) to detect the macrophage phenotypes.

Quantitative polymerase chain reaction (qPCR). Total RNA was purified from BMDMs using TRIzol (Vazyme, Nanjing, China). 1 μg RNA was reverse transcribed with HiScript II Q RT SuperMix for qPCR (Vazyme, Nanjing, China), and qPCR was performed using 2× ChamQ Universal SYBR qPCR Master Mix (Vazyme, Nanjing, China) on CFX96 and CFX384 systems (Bio-Rad, USA). The primer sequences are listed in SI Table S1. The relative expression levels were quantitatively determined using the $2^{-\Delta\Delta CT}$ method.

Western blot (WB). Ice-cold radioimmunoprecipitation assay (RIPA) lysis buffer (Solarbio, Beijing, China) supplemented with 1% phenylmethanesulfonyl fluoride (Beyotime, Shanghai, China), protein phosphatase inhibitor (Solarbio, Beijing, China), and protease inhibitor mixture (Solarbio, Beijing, China) was applied on BMDMs to obtain protein samples. The protein samples were separated by sodium dodecyl sulfate–polyacrylamide gel electrophoresis and transferred to polyvinylidene fluoride membranes. The membranes were blocked with 5% skim milk, incubated with primary antibodies including nuclear factor-κB (NF-κB, 1 : 5000, Proteintech, 80979-1-RR), phosphorylated NF-κB p65 (Ser536) (p-NF-κB, 1 : 1000, Cell Signaling Technology, 3033) and GAPDH (1 : 5000, Proteintech, 60004-1-Ig) overnight at 4 °C, and then incubated with horseradish peroxidase (HRP) conjugated goat anti-rabbit secondary antibody (1 : 5000, Jackson ImmunoResearch, 111-035-003) after washing. Protein bands were visualized by enhanced chemiluminescence (Millipore, USA) and photographed using a ChemiDoc Touch Imaging System (Bio-Rad, USA).

2.8. In vitro cell proliferation assay

The proliferation of HESCs was investigated by culturing with the hydrogels in a Transwell chamber using the CCK-8 assay. HESCs were seeded in a 24-well plate at a density of 1×10^4 cells per well and cultured for 24 h at 37 °C. The experimental groups were set as follows: ① Control group; ② H group; ③

HM group; and ④ HME group. At preset times, the cell viability was tested using the CCK-8 method.

2.9. In vivo establishment of a rat endometrial damage model

Animal experiments were approved by the Animal Ethics Committee of Zhejiang University and the Ethics Committee of Sir Run Run Shaw Hospital, Zhejiang University School of Medicine (ethics no.: SRRSH202402295). All experimental female Sprague Dawley rats (SD rats, 250 g, 9 weeks old) were purchased from Zhejiang Academy of Medical Sciences. SD rats were intraperitoneally anesthetized and disinfected with iodophor. An incision was made along the ventral midline to find the uterus. An incision of the uterine horn was made close to the vagina, and the other end close to the ovary was secured with hemostatic forceps. 95% ethanol was injected and filled the uterine horn, lasting for 90 s. Subsequently, the uterine horn was thoroughly rinsed with PBS. The rats were divided as follows: ① Natural repair (NR) group: no subsequent treatment was given after injury; ② H group: 100 μL hydrogel precursor solution was injected; ③ HM group: 100 μL hydrogel precursor solution containing MnO$_2$ NPs; and ④ HME group: 100 μL hydrogel precursor solution containing 200 μg mL^{-1} MnO$_2$@E2 NPs. Since we regarded MnO$_2$@E2 NPs as a whole and the efficacy of E2 in IUA has been confirmed and widely recognized, no additional E2 group was set in the animal experiments. After treatment, the wound was sutured.

2.10. Histological, immunohistochemical and immunofluorescence evaluation

SD rats were euthanized and uterine tissues were collected for paraffin embedding. Histological evaluation included H&E staining and Masson's trichrome staining, immunohistochemical staining of estrogen receptor (ER, 1 : 1000, Abcam, ab32063) and immunofluorescence staining of F4/80 (1 : 2000, Proteintech, 29414-1-AP), CD86 (1 : 200, Proteintech, 13395-1-AP), CD163 (1 : 100, Proteintech, 16646-1-AP) and 4-HNE (1 : 400, Abcam, ab46545), and images were analyzed using Image J.

2.11. Fertility test

To evaluate the effect of the HME on fertility recovery, 42 female SD rats were employed for the experiment. The endometrial injury model was established on the right uterine horn, which was further treated, while the left horn with no extra treatment was set as the normal control group. After 45 days of repair, all female SD rats were mated with proven fertile male SD rats. The appearance of the vaginal plugs indicated gestational day (GD) 1 and the rats were euthanized at GD 16. The number of embryos and the pregnancy rate of the rats were analyzed.

2.12. Real-time quantitative polymerase chain reaction (RT-qPCR)

Total RNA of the uterine samples at 3 d and 7 d after the operation was extracted and reverse transcribed into cDNA using

the All-in-One First-Strand cDNA Synthesis SuperMix for qPCR Kit (TransGen Biotech, Beijing, China). The quantitative PCR reaction was determined using SYBR Green qPCR Master Mix Kit (APExBIO, USA). Using GAPDH as an internal reference, the relative expression levels were quantitatively determined by the $2^{-\Delta\Delta CT}$ method. The primer sequences are listed in SI Table S2.

2.13. Statistical analysis

The data (presented as mean ± SD) were evaluated by one-way analysis of variance (ANOVA) following Tukey's *post hoc* test, and Fisher's exact test was applied to analyze the fertility results of relative embryo implantation using GraphPad Prism. Significance levels were set as * for $p < 0.05$, ** for $p < 0.01$, and *** for $p < 0.001$.

3. Results and discussion

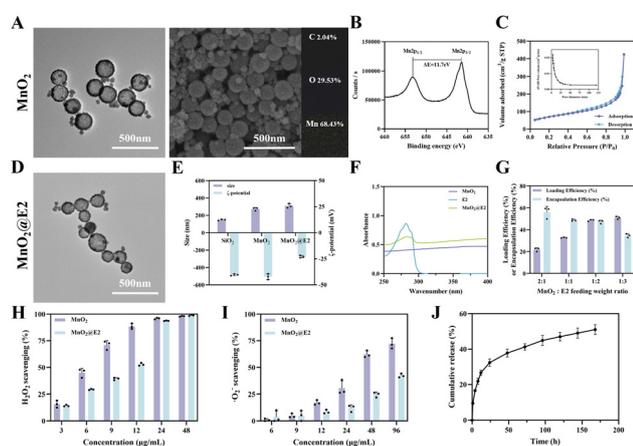### 3.1. Characterization of MnO_2 and MnO_2@E2 NPs

Firstly, TEM and SEM images (Fig. 1A) showed that the MnO_2 NPs possessed a rough hollow spherical structure with an average size of 182.8 nm. XPS fine scanning of the Mn 2p and Mn 3s orbitals of the MnO_2 NPs (Fig. 1B and Fig. S1A) revealed two peaks at the binding energies of 653.2 eV and 641.5 eV, corresponding to Mn $2p_{1/2}$ and Mn $2p_{3/2}$, respectively.[32,33] Combined with the FT-IR spectrum (Fig. S1B) and XRD pattern (Fig. S1C), the NPs were identified as MnO_2. The nitrogen adsorption–desorption isotherm and the pore size distribution plot (Fig. 1C) proved the presence of mesopores with an average size of 10.6 nm in MnO_2. The presence of mesoporous

and hollow structures increased the specific surface area of the NPs, which is conducive to the efficient loading of drugs.

After drug loading, the MnO_2@E2 NPs were obtained. TEM (Fig. 1D) and SEM (Fig. S2) images showed that their morphology remained the same as that of MnO_2 NPs. The MnO_2@E2 NPs had a particle size of 309.9 nm and a zeta potential of −22.9 mV (Fig. 1E). Fig. 1F and Fig. S1B revealed the successful loading of E2. To screen the optimal conditions, their drug loading properties were tested (Fig. 1G). Considering the utilization rate of E2, the feeding ratio of 1 : 1 was finally selected, while the loading efficiency of MnO_2@E2 NPs was 32.7% and the encapsulation efficiency was 48.7%. H_2O_2 and $\cdot O_2^-$ are important ROS inducing oxidative stress, thus tests on their scavenging were conducted. Fig. 1H and I displayed that the MnO_2 NPs and MnO_2@E2 NPs showed good concentration-dependent scavenging ability, respectively. The drug release profile of MnO_2@E2 NPs in a neutral environment (Fig. 1J) showed that E2 was released rapidly initially, gradually slowed down and entered the plateau phase of 51.1%, proving that the MnO_2 NPs are good nanocarriers for sustained release.

3.2. Characterization of the HME

The ^1H NMR spectra (Fig. S3) showed that the degree of substitution of HA-A and HA-F were 33% and 39%. Fig. 2A showed that the precursor solution was injectable before gelation through the D–A reaction. From the SEM images (Fig. 2B and Fig. S4), H and HME exhibited three-dimensional network

Fig. 1 Characterization of MnO_2 and MnO_2@E2 NPs. (A) TEM, SEM and EDS elemental mapping images of MnO_2 NPs. (B) XPS spectrum of Mn 2p of MnO_2 NPs. (C) Pore-size distribution curve (inset) and N_2 adsorption/desorption isotherm of MnO_2 NPs. (D) TEM image of MnO_2@E2 NPs. (E) Particle size and zeta potential of SiO_2, MnO_2 and MnO_2@E2 NPs ($n = 3$). (F) UV-vis spectra of MnO_2 NPs, E2 and MnO_2@E2 NPs. (G) E2 loading properties in MnO_2 NPs at different MnO_2 : E2 feeding weight ratios ($n = 3$). (H) H_2O_2 and (I) $\cdot O_2^-$ scavenging efficiency of MnO_2 and MnO_2@E2 NPs ($n = 3$). (J) *In vitro* E2-release property of MnO_2@E2 NPs in a neutral environment ($n = 3$).
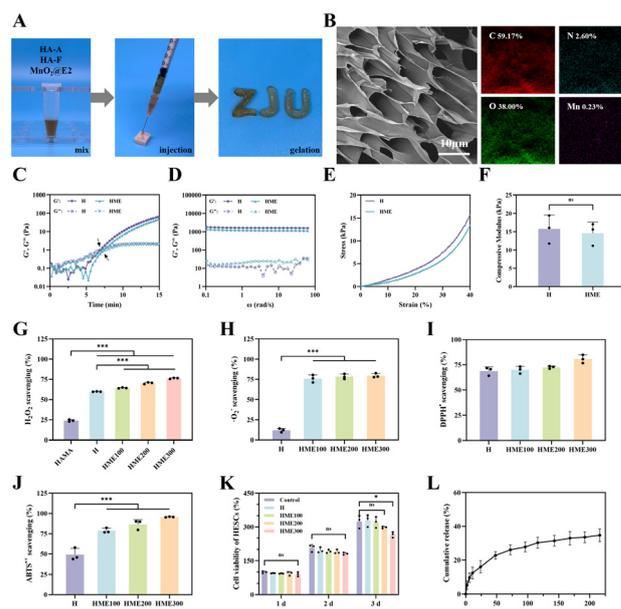
Fig. 2 Characterization of the HME. (A) Injectability and gelation process. (B) SEM and EDS elemental mapping images of the HME. (C) Time sweeping and (D) frequency sweeping tests. (E) Stress–strain curves and (F) compression moduli ($n = 3$). (G) H_2O_2, (H) $\cdot O_2^-$, (I) DPPH$\cdot$ and (J) ABTS$^{\cdot+}$ scavenging efficiency of the hydrogels ($n = 3$). (K) Cell viability of HESCs cultured with the hydrogel extracts ($n = 3$). (L) *In vitro* release of E2 from the HME in a neutral environment ($n = 3$).

structure with uniform pore size, and the increase in the proportion of M, N, and C elements of the HME also confirmed the incorporation of MnO_2@E2 NPs.

To achieve injectability, the precursor solution is required to crosslink rapidly in the physiological environment. Therefore, a time scanning test (Fig. 2C) of rheological properties was first carried out, showing that the storage modulus (G') and the loss modulus (G'') of the precursor solution started at a small value with $G' < G''$, where the system exhibited fluid-like characteristics. As the reaction proceeded, the time point of $G' = G''$ was defined as the gelation time (t_c),[34] representing the transformation of the system to solid-like behavior.[35] The t_c of the hydrogel was about 7 min. Fig. 2D showed that G' was greater than G'', independent of the applied frequency, which marked the formation of the hydrogel.[35]

The designated application scenario is the uterine cavity, while the elastic modulus of the endometrium is about 250 Pa.[36] The mechanical tests, as shown in Fig. 2E, showed that as the strain increased, the stress also increased. The compression modulus of H was 15.8 kPa, and that of the HME was 14.6 kPa (Fig. 2F). Compared with intrauterine devices and scaffolds in IUA treatment, the HME possessed closer mechanical properties to the usage scenario and reduced the compression of tissues.

The swelling ratios of H and HME (Fig. S5) indicated that the hydrogels had excellent swelling property, which indicated their potential to absorb excess tissue exudate *in vivo*.

3.3. Antioxidation properties, drug release behavior, cytocompatibility and degradation properties of the HME

The formula of HA-A and HA-F in the HME referred to a previous work.[24] Additionally, it is necessary to optimize the antioxidant capacity based on biocompatibility, mainly by adjusting the concentration of MnO_2@E2 NPs for the treatment of IUA.

Firstly, the antioxidant properties of HME were examined from multiple aspects. Fig. 2G–J showed that the hydrogels exhibited scavenging abilities for H_2O_2, $^•O_2^-$, DPPH$^•$ and ABTS$^{•+}$, with the activity increasing in a concentration-dependent manner for the MnO_2@E2 NPs. It could be concluded that H itself had certain antioxidant properties against H_2O_2, DPPH$^•$ and ABTS$^{•+}$, which might be attributed to the reduction properties conferred by the modified groups of HA. There were significant differences among the methacrylated hyaluronic acid hydrogel (HAMA) group, H group and HME group in H_2O_2 scavenging ability (Fig. 2G). The addition of MnO_2@E2 NPs significantly enhanced the $^•O_2^-$ scavenging ability of the hydrogel (Fig. 2H). DPPH$^•$ and ABTS$^{•+}$ are free radicals often used to detect the antioxidant properties of hydrogels, which were explored subsequently. The scavenging rate of DPPH$^•$ for all the groups reached 70%, and the scavenging rate of ABTS$^{•+}$ for HME200 was 86.5%, which further indicated that the incorporation of MnO_2@E2 NPs was beneficial to improve the antioxidant properties of the hydrogels.

We demonstrated the biocompatibility of the hydrogels through cytotoxicity firstly for their further application *in vivo*. The results (Fig. 2K) showed that there were no significant differences among the groups at 1 d and 2 d. Though the *P*-value between the control and HME300 group was less than 0.05 at 3 d, HME generally demonstrated good cellular safety.

Based on the above-mentioned experimental results, HME200 was finally selected as the subsequent experimental group and abbreviated as HME in the following text.

The hydrogel was anticipated for implantation without secondary surgery, which meant that its degradation properties were of great significance. Under the influence of hyaluronidase, HME gradually disintegrated and degraded completely at 30 d (Fig. S6A). Fig. S6B showed that the MnO_2@E2 NPs in HME could be decomposed to soluble Mn^{2+}, and the decomposition rate of MnO_2@E2 NPs was significantly accelerated under the conditions of 100 μM H_2O_2 and pH = 5. This indicated that the HME possessed appropriate degradation properties and could be excreted from the body.

E2 was loaded in the hydrogel for long-term release to promote endometrial repair, and its release kinetic curves could reflect its effective treatment duration. The E2-release profile from the HME in a neutral environment (Fig. 2L) matched that from the MnO_2@E2 NPs, but its sustained release from the former was more effective and reached a plateau later. The combination of the hydrogel and MnO_2 NPs provided a platform for sustained drug release, which is beneficial for reducing the biological toxicity and prolonging the effective time of the drug *in vivo*.
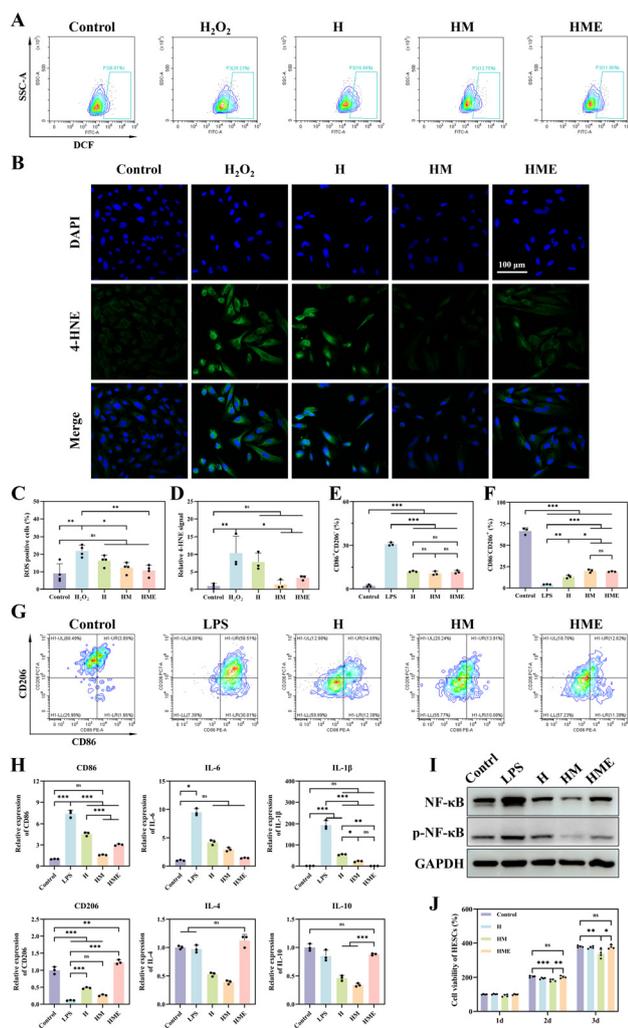
3.4. Intracellular antioxidation properties, regulatory effect on the phenotype of macrophages and cell proliferation of the HME

To select the effective concentration of H_2O_2, the cell viability of HESCs under different H_2O_2 concentrations was first investigated. The results (Fig. S7A) showed that cell viability was dose-dependent on H_2O_2 concentration. The *P*-values among the HME 100 and 200 groups and the control group were all less than 0.001. Therefore, 100 μM was ultimately chosen as the experimental condition. Furthermore, Fig. S7B showed that HME was conducive to maintaining the cell viability of HESCs under H_2O_2, whose effect was generally dependent on the concentration of MnO_2@E2 NPs.

The antioxidant properties of HME were verified previously and further investigated at the cellular level in this section. Firstly, the ability of the hydrogels to scavenge intracellular ROS was tested. Representative images of the ROS positive rate of HESCs and the quantitative analysis (Fig. 3A and C, respectively) illustrated that the levels of ROS in the H, HM, and HME groups decreased in turn compared with the H_2O_2 group, manifesting that the ability of ROS scavenging in the hydrogel groups increased, especially in the HM and HME groups, which is attributed to the MnO_2 nanozyme.

Moreover, the degree of oxidative stress damage caused by ROS to HESCs was evaluated by immunofluorescence staining of 4-HNE. 4-HNE is a marker of lipid peroxidation and cyto-

Fig. 3 *Intracellular* antioxidation properties, the regulatory effect on the phenotype of macrophages and cell proliferation of the HME. (A) Representative flow cytometry plots of ROS-positive cells (%) of HESCs cultured with the hydrogels and (C) quantitative analysis (*n* = 4). (B) Representative 4-HNE immunofluorescence images of HESCs after different treatments and (D) quantified analysis results (*n* = 3). (E) and (F) quantitative analysis of the ratio of CD86 and CD206 positive cells (%) of BMDMs cultured with the hydrogels (*n* = 3) and (G) representative flow cytometry plots. (H) Relative expression of CD86, pro-inflammatory cytokines (IL-6 and IL-1β), CD206, and anti-inflammatory cytokines (IL-4 and IL-10) of BMDMs after different treatments (*n* = 3) by qPCR. (I) Western blot analysis of BMDMs with different treatments, including p-NF-κB, NF-κB and GAPDH. (J) CCK-8 assay assessing HESC proliferation with different treatments (*n* = 4).

toxicity induced by oxidative stress.[37] Representative confocal fluorescence images and the relative fluorescence intensity (Fig. 3B and D, respectively) showed that the oxidative stress model was successfully established and the fluorescence intensity of the HME group weakened, indicating that it could protect cells from oxidative stress damage.

The intracellular ROS scavenging experiment simulated an environment with a high concentration of ROS, while the intracellular oxidative stress damage reduction experiment further

simulated the cell conditions after oxidative stress, extending the former experiment in the time dimension. It could be concluded that the hydrogels had a certain degree of intracellular antioxidant capacity, which protected HESCs from damage by ROS.

To further evaluate the effect of the hydrogels on phenotype polarization, the expression of CD86 (marker for M1 phenotype) and CD206 (marker for M2 phenotype) on the surface of BMDMs was detected by flow cytometry analysis (Fig. 3G). A significant decrease in the ratio of CD86$^+$CD206$^-$ macrophages (Fig. 3E) and an increase in the ratio of CD86$^-$CD206$^+$ macrophages (Fig. 3F) in the hydrogel groups were observed, especially HM and HME, compared with the LPS group. Specifically, Fig. S8 shows similar trends in CD86 and CD206 positive cells, while the expression of CD206 in the hydrogel groups was lower than the LPS group. Finally, the expression of CD86, pro-inflammatory cytokines (IL-6 and IL-1β), CD206 and anti-inflammatory cytokines (IL-4 and IL-10) was analyzed by qPCR (Fig. 3H). The trends in the variation of CD86 and CD206 in each group were consistent with those in the flow cytometry analysis. The expression levels of IL-6 and IL-1β of HME weakened compared with the LPS group, which revealed that HME was capable of alleviating inflammation. Besides, there was no significant difference in IL-4 and IL-10 between HME and the control group. These results proved that HME could inhibit pro-inflammatory responses and achieve anti-inflammatory effects to a certain extent.

To explore the relevant signaling pathway regulating macrophages, a WB experiment on BMDMs was carried out. NF-κB is a key mediator regulating innate and adaptive immune responses, which may enhance the expression of pro-inflammatory cytokines.[38,39] NF-κB usually refers to the inactive state that binds to the inhibitor of NF-κB (IκB), while p-NF-κB indicates the activation of the NF-κB pathway. Fig. 3I shows the upregulation of p-NF-κB expression in the LPS group, indicating that intracellular inflammation was induced. The expression of p-NF-κB was significantly reduced after treatment with the HM and HME. Alternatively, the expression of NF-κB in the hydrogel groups relatively decreased compared with the LPS group. In general, the role of HME in alleviating the inflammatory response of M1-phenotype BMDMs may be achieved by regulating the NF-κB signaling pathway.

The effect of E2 on the proliferation of HESCs was examined. Fig. 3J shows that at 2 d and 3 d, the cell viability of HME was significantly better than that of HM, with no significant difference with the control group, which demonstrated that the introduction of E2 had a relatively proliferative effect on HESCs.

3.5. HME promoted endometrial repair in a rat endometrial damage model

Methods for establishing an endometrial injury model include mechanical damage,[40] electrical burns and chemical damage.[41] However, most of these methods are complex and unstable. In contrast, 95% ethanol perfusion can not only effectively induce the development of IUA but also maintain

the sample stability.[42] Therefore, the 95% ethanol perfusion method was ultimately selected for use.

Firstly, we tested the biocompatibility of the HME group in rats. Fig. S9 shows that there was no distinct toxicity, inflammation or edema indication in the HME group compared with the control group, which met the basic requirements for *in vivo* implantation.

Furthermore, the uterine tissues were collected for histological and immunohistochemical evaluation. The morphology of the uterine tissue is shown in Fig. S10. The *in vivo* degradation profile of HME (Fig. S11) showed that the HME gradually degraded and no hydrogel residue was detected at 45 d. In the later stages, the blockage and edema caused by IUA in the NR group became severe, which did not exist in the other groups. At 15 d, 30 d and 45 d, the endometrial thickness of HM and HME groups slightly increased compared to the NR group (Fig. 4B and C). There was a significant difference between HME and NR groups at 30 d. At 45 d, HME and H were significantly different, indicating that MnO$_2$@E2 NPs were beneficial for promoting endometrial thickening through eliminating ROS and E2 release. Glands are important secretory structures in the endometrium, which can secrete active substances and participate in regulating embryo implantation.[43] Fig. 4D shows that hydrogels increased the number of endometrial glands, and there were significant differences in HME and NR groups at 15 d, 30 d and 45 d, manifesting that HME could stimulate the formation of endometrial glands. Besides, the fact that glands did not invade the endometrial myometrium proved that the phenomenon was not pathological proliferation. Masson's trichrome staining (Fig. 4E and F) displayed that there were significant differences between each experimental group and the NR group, revealing that the implantation of the hydrogels was generally beneficial for reducing collagen deposition and the fibrotic area. ER is an essential secretory structure in the endometrium, with which E2 binds and exerts a regulatory effect on uterine physiological activity.[44] After selecting endometrial tissue areas with minimal influence from luminal and glandular epithelium, Fig. S12 and Fig. 4G show that the ER-positive area in the HME had significant differences with the NR group, indicating that the HME was conducive to accelerating the regeneration of ER as repair proceeded. Overall, the above-mentioned experimental results have demonstrated in multiple dimensions that the composite hydrogels have recovery effect on the structure and function repair of the endometrium.

3.6. Effect of HME on fertility recovery

The fertility recovery test is an important indicator to evaluate uterine functional repair after IUA. Therefore, the pregnancy rate and the number of embryos in the right uteri of the rats were checked at GD 16. Fig. 5A shows representative images of the uterine horn of each group. The left uterine horn as the control group achieved the implantation of embryos, while the number of embryos in the right uterine horn was affected by the treatments, as shown in Fig. 5B and Table S3. Compared with 9.1% for the NR group, the right uterine pregnancy rates
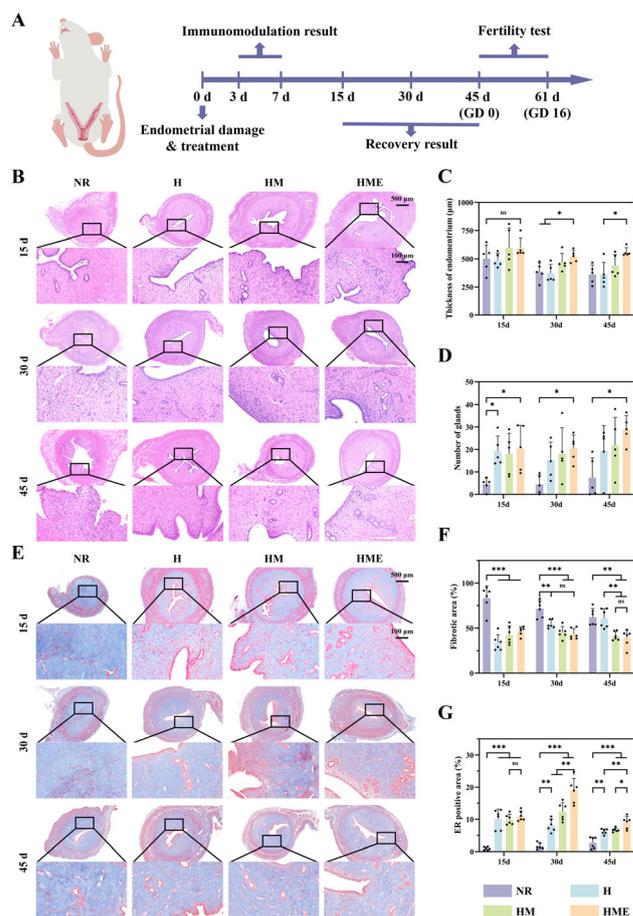
Fig. 4 Endometrial repair in a rat endometrial damage model. (A) Schematic diagram of the animal experiment setup. (B) Representative images of H&E staining and quantitative analysis of (C) endometrial thickness (n = 5) and (D) number of glands (n = 5) in uteri at 15 d, 30 d and 45 d after different treatments. (E) Representative images of Masson's trichrome staining and (F) quantitative analysis of the endometrial fibrotic area (n = 6). (G) Quantitative analysis of ER-positive area by immunohistochemical staining (n = 6).

Fig. 5 Effect of HME on fertility recovery. (A) Representative morphological images of the uterine horns and (B) violin plot analysis of embryo number in right uteri after different treatments at GD 16 (n = 11 in the NR group, n = 10 in the H group, n = 10 in the HM group, and n = 11 in the HME group).

for HM and HME groups increased to 40% and 45.5%, respectively. The number of right uterine embryos in the HME also increased compared with that in the NR group, as reflected by the significant increase in relative embryo implantation;

however, there was no significant difference in the number of right uterine embryos. In addition, the difference in abortion rate (Table S4) in the right uteri among the different groups was not significant. Generally, the HME might be beneficial to fertility recovery of the uterus.

3.7. *In vivo* immunomodulation of HME

After endometrial damage, excessive ROS will be generated, forming an oxidative stress microenvironment, which causes harm to HESCs. The oxidative stress microenvironment ultimately triggers inflammatory responses and induces macrophages to the M1 phenotype, releasing inflammatory factors and intensifying local inflammatory responses.

Therefore, the protective effect of the hydrogels on tissues under oxidative stress conditions was evaluated first. The expression of 4-HNE at 3 d postoperatively was detected by immunofluorescence staining. As shown in Fig. 6A and B, the relative fluorescence intensities of the H, HM and HME groups decreased to varying degrees, showing significant differences from the NR group, which indicated that based on the regulatory effect on oxidative stress of H, the addition of MnO_2 and MnO_2@E2 NPs further enhanced the ability of the HM and HME to protect tissues from oxidative stress damage.
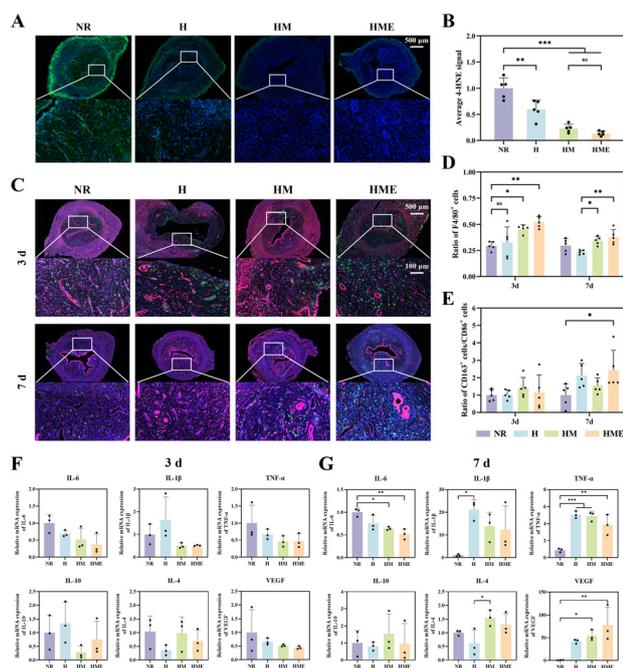
Fig. 6 *In vivo* immunomodulation by the HME. (A) Representative immunofluorescence images of 4-HNE of HESCs after different treatments and (B) quantitative analysis (*n* = 5). (C) Representative immunofluorescence images of macrophages co-stained with F4/80 (green), CD86 (red), and CD163 (pink) at 3 d and 7 d after different treatments. Quantified statistical analysis results of (D) ratio of F4/80^{+} cells and (E) ratio of CD 163^{+} cells relative to CD86^{+} cells (*n* = 5). Relative expression levels of cytokines (pro-inflammatory cytokines: IL-6, IL-1β and TNF-α; anti-inflammatory cytokines: IL-10 and IL-4 and the angiogenic factor: VEGF-A) in uteri at (F) 3 d and (G) 7 d after different treatments (*n* = 3).

To evaluate the effect of the hydrogels on the phenotype polarization of macrophages in the endometrium, the expression of F4/80 (marker for macrophages), CD86 (marker for M1 phenotype), and CD163 (marker for M2 phenotype) at 3 d and 7 d after surgery was detected by immunofluorescence staining. After collecting the endometrial tissue areas with minimal influence from luminal and glandular epithelium, representative fluorescence images (Fig. 6C) and analysis results (Fig. 6D) demonstrated that the fluorescence intensity of F4/80 in the HME group enhanced compared to the NR group, indicating that the HME might recruit macrophages. At 7 d, there was a significant difference in the proportion of CD163 cells to CD86 cells (Fig. 6E) between the HME and NR groups, underlining that HME could regulate macrophages by increasing the ratio of M2 to M1 phenotype, which might be conducive to the transition from inflammatory to the remodeling and regeneration phases of tissues.

To evaluate the effect of the hydrogels on cytokine secretion, the relative expression levels of pro-inflammatory factors (IL-6, IL-1β, and TNF-α), anti-inflammatory factors (IL-10 and IL-4), and vascular endothelial growth factor (VEGF-A) at 3 d and 7 d after surgery were detected by RT-qPCR. As shown in Fig. 6F, the expression levels of IL-6, IL-1β and TNF-α at 3 d in NR and hydrogel groups (H, HM and HME) decreased generally, implying that the uterine pro-inflammatory microenvironment was suppressed by the hydrogels. However, anti-inflammatory factors and VEGF-A did not show patterns. As shown in Fig. 6G, the expression levels of IL-6 of HME at 7 d were significantly lower than those in the NR group, while IL-1β and TNF-α in the hydrogel groups were higher, which might be attributed to the foreign body reaction triggered by incompletely degraded hydrogels. The expression of IL-4 in the HM and HME slightly increased. The complex expression of cytokines is associated with physiological environments and immune mechanisms. Additionally, HME possessed the ability to promote the secretion of VEGF-A, resulting in a significantly higher expression level compared with the NR group, indicating its pro-angiogenic potential. In general, HME had a regulatory effect on the secretion of cytokines.

Conclusions

In summary, from the perspective of pathogenesis of IUA, we constructed an MnO_2@E2 NP-powered injectable hydrogel system to regulate the inflammatory microenvironment of the uterus after IUA. The hydrogel exhibited an appropriate gelation time, mechanical properties, antioxidant activity and biocompatibility. *In vitro* experiments demonstrated that the HME could eliminate *intracellular* ROS, alleviate cellular damage under oxidative stress, regulate the phenotype of macrophages through the NF-κB signaling pathway and promote the proliferation of HESCs. In a rat endometrial injury model, HME could regulate inflammatory responses and improve the endometrial microenvironment to a certain extent through MnO_2 in the

inflammatory stage and releasing the drug E2 to stimulate the regeneration and repair of the endometrial structure and function, and even influence the recovery of fertility. This hydrogel integrating multiple functions shows research and application potential for IUA treatment from the perspective of pathogenesis.

Author contributions

Ying Xu and Zi Ye: writing – original draft, conceptualization, methodology, validation, data curation, visualization. Sentao Hu, Lichao Chu, Wangyan He: investigation. Liaobing Xin, Weijun Tong, Songying Zhang: funding acquisition, project administration. Lie Ma: writing – review & editing, conceptualization, supervision, funding acquisition, project administration.

Conflicts of interest

The authors declare that they have no known competing financial interests or personal relationships that could have appeared to influence the work reported in this paper.

Data availability

The data that support the findings of this study are available from the corresponding author upon reasonable request.

Supplementary information (SI) including part of experimental section and results is available. See DOI: https://doi.org/10.1039/d6bm00109b.

Acknowledgements

References

1 X. Santamaria, K. Isaacson and C. Simon, *Hum. Reprod.*, 2018, **33**(8), 1374–1380.
2 A. Owusu-Akyaw, K. Krishnamoorthy, L. T. Goldsmith and S. S. Morelli, *Hum. Reprod. Update*, 2019, **25**(1), 114–133.
3 Y.-T. Song, P.-C. Liu, J. Tan, C.-Y. Zou, Q.-J. Li, J. Li-Ling and H.-Q. Xie, *Stem Cell Res. Ther.*, 2021, **12**(1), 556.
4 A. Rodriguez-Eguren, C. Bueno-Fernandez, M. Gomez-Alvarez, E. Frances-Herrero, A. Pellicer, J. Bellver, E. Seli and I. Cervello, *Hum. Reprod. Update*, 2024, **30**(5), 584–613.
5 L. Xin, X. Lin, Y. Pan, X. Zheng, L. Shi, Y. Zhang, L. Ma, C. Gao and S. Zhang, *Acta Biomater.*, 2019, **92**, 160–171.
6 L. Xin, X. Lin, F. Zhou, C. Li, X. Wang, H. Yu, Y. Pan, H. Fei, L. Ma and S. Zhang, *Acta Biomater.*, 2020, **113**, 252–266.
7 D. Yu, Y.-M. Wong, Y. Cheong, E. Xia and T.-C. Li, *Fertil. Steril.*, 2008, **89**(4), 759–779.
8 X. Santamaria, K. Isaacson and C. Simon, *Hum. Reprod.*, 2018, **33**(8), 1374–1380.
9 X. Peng, T. Wang, B. Dai, Y. Zhu, M. Ji, P. Yang, J. Zhang, W. Liu, Y. Miao, Y. Liu, S. Wang and J. Sun, *Adv. Sci.*, 2025, **12**(1), 2410769.
10 H. Sun, J. Dong, Z. Fu, X. Lu, X. Chen, H. Lei, X. Xiao, S. Chen, J. Lu, D. Su, Y. Xiong, Z. Fang, J. Mao, L. Chen and X. Wang, *Adv. Mater.*, 2024, **36**(21), 2308921.
11 L. Feng, L. Wang, Y. Ma, W. Duan, S. Martin-Saldana, Y. Zhu, X. Zhang, B. Zhu, C. Li, S. Hu, M. Bao, T. Wang, Y. Zhu, F. Yang and Y. Bu, *Bioact. Mater.*, 2023, **27**, 82–97.
12 D. Zhang, L. Li, J. Zhou, X. Wang, X. Gao, J. Chen, T. Duan, Q. Ma, J. Li, Y. Yu and Q. Zhou, *Chem. – Eng. J.*, 2025, **512**, 162672.
13 J. Meng, L. Xin, J. Dong, S. Ren, Y. Cao, Y. Liang, X. Zhang and R. Zhang, *ACS Appl., Mater. Interfaces*, 2025, **17**(31), 44188–44198.
14 Y. Liang, J. Meng, Z. Yu, Y. Guo, X. Zhang, Y. Yan, S. Du, S. Jin, J. Li, H. Yang, X. Zhang, Z. Liu, L. Li and J. Xie, *Biomaterials*, 2025, **315**, 122923.
15 C. Li, Z. Zhao, Y. Luo, T. Ning, P. Liu, Q. Chen, Y. Chu, Q. Guo, Y. Zhang, W. Zhou, H. Chen, Z. Zhou, Y. Wang, B. Su, H. You, T. Zhang, X. Li, H. Song, C. Li, T. Sun and C. Jiang, *Adv. Sci.*, 2021, **8**(20), 2101526.
16 A. Dhall and W. Self, *Antioxidants*, 2018, **7**(8), 97.
17 X. Tang, X. Yang, Y. Yu, M. Wu, Y. Li, Z. Zhang, G. Jia, Q. Wang, W. Tu, Y. Wang, X. Zhu and S. Li, *J. Nanobiotechnol.*, 2024, **22**(1), 125.
18 L. He, G. Huang, H. Liu, C. Sang, X. Liu and T. Chen, *Sci. Adv.*, 2020, **6**(12), eaay9751.
19 D. Xu, L. Wu, H. Yao and L. Zhao, *Small*, 2022, **18**(37), 2203400.
20 K. Xiang, H. Wu, Y. Liu, S. Wang, X. Li, B. Yang, Y. Zhang, L. Ma, G. Lu, L. He, Q. Ni and L. Zhang, *Theranostics*, 2023, **13**(8), 2721–2733.
21 T. Ye, C. Chen, D. Wang, C. Huang, Z. Yan, Y. Chen, X. Jin, X. Wang, X. Ding and C. Shen, *Nat. Commun.*, 2024, **15**(1), 1682.
22 Y. Cao, K. Cheng, M. Yang, Z. Deng, Y. Ma, X. Yan, Y. Zhang, Z. Jia, J. Wang, K. Tu, J. Liang and M. Zhang, *J. Nanobiotechnol.*, 2023, **21**(1), 21.
23 J. Zhao, W. Gao, X. Cai, J. Xu, D. Zou, Z. Li, B. Hu and Y. Zheng, *Theranostics*, 2019, **9**(10), 2843–2855.
24 S. Hu, Y. Dai, L. Xin, X. Zheng, Z. Ye, S. Zhang and L. Ma, *Acta Biomater.*, 2024, **177**, 77–90.
25 L. Kou, X. Jiang, S. Xiao, Y.-Z. Zhao, Q. Yao and R. Chen, *J. Control. Release*, 2020, **318**, 25–37.
26 S. Vasvani, P. Kulkarni and D. Rawtani, *Int. J. Biol. Macromol.*, 2020, **151**, 1012–1029.
27 X. Xie, R. Xu, H. Ouyang, S. Tan, C. Guo, X. Luo, Y. Xie, D. Wu, X. Dong, J. Wu, Y. Wang and L. Zhao, *J. Mater. Chem. B*, 2022, **10**(42), 8684–8695.
28 S.-S. Zhang, W.-T. Xia, J. Xu, H.-L. Xu, C.-T. Lu, Y.-Z. Zhao and X.-Q. Wu, *Int. J. Nanomed.*, 2017, **12**, 5643–5657.

29 E. D. Albrecht, J. S. Babischkin, Y. Lidor, L. D. Anderson, L. C. Udoff and G. J. Pepe, *Hum. Reprod.*, 2003, **18**(10), 2039–2047.

30 P. P. Ghimire and M. Jaroniec, *J. Colloid Interface Sci.*, 2021, **584**, 838–865.

31 Y. Dai, L. Xin, S. Hu, S. Xu, D. Huang, X. Jin, J. Chen, R. W. S. Chan, E. H. Y. Ng, W. S. B. Yeung, L. Ma and S. Zhang, *Regen. Biomater.*, 2023, **10**, rbad080.

32 M. C. Biesinger, B. P. Payne, A. P. Grosvenor, L. W. M. Lau, A. R. Gerson and R. S. C. Smart, *Appl. Surf. Sci.*, 2011, **257**(7), 2717–2730.

33 J. Fei, Y. Cui, X. Yan, W. Qi, Y. Yang, K. Wang, Q. He and J. Li, *Adv. Mater..*, 2008, **20**(3), 452–456.

34 G. Stojkov, Z. Niyazov, F. Picchioni and R. K. Bose, *Gels*, 2021, **7**(4), 255.

35 N. Sahiner, M. Singh, D. De Kee, V. T. John and G. L. McPherson, *Polymer*, 2006, **47**(4), 1124–1131.

36 Y. Abbas, A. Carnicer-Lombarte, L. Gardner, J. Thomas, J. J. Brosens, A. Moffett, A. M. Sharkey, K. Franze, G. J. Burton and M. L. Oyen, *Hum. Reprod.*, 2019, **34**(10), 1999–2008.

37 Y. Li, T. Zhao, J. Li, M. Xia, Y. Li, X. Wang, C. Liu, T. Zheng, R. Chen, D. Kan, Y. Xie, J. Song, Y. Feng, T. Yu and P. Sun, *J. Immunol. Res.*, 2022, **2022**, 2233906.

38 G. Bonizzi and M. Karin, *Trends Immunol.*, 2004, **25**(6), 280–288.

39 K. Taniguchi and M. Karin, *Nat. Rev. Immunol.*, 2018, **18**, 309–324.

40 Q. Feng, B. Gao, X. Zhao, H. Huang, S. Yi, L. Zou, X. Liu, M. Xue and D. Xu, *Ann. Transl. Med.*, 2020, **8**(4), 56.

41 F. Liu, Z.-J. Zhu, P. Li and Y.-L. He, *J. Surg. Res.*, 2013, **183**(1), 296–303.

42 P. C. Liu, Y. T. Song, L. M. Zhao, Y.-L. Jiang, J. G. Hu, L. Dong, X.-l. Zhou, L. Zhou, Y. Li, J. Li-Linge and H. Q. Xie, *Heliyon*, 2024, **10**(3), e25365.

43 G. J. Burton and E. Jauniaux, *Proc. R. Soc. B Biol. Sci.*, 2023, **290**(1997), 20230191.

44 M.-A. Arevalo, I. Azcoitia and L. M. Garcia-Segura, *Nat. Rev. Neurosci.*, 2015, **16**(1), 17–29.